PHYSICAL REVIEW B **97**, 104303 (2018)

# Contributions of different degrees of freedom to thermal transport in the $C_{60}$ molecular crystal

Sushant Kumar,[1] Cheng Shao,[1,2] Simon Lu,[1] and Alan J. H. McGaughey[1,*]
[1]*Department of Mechanical Engineering, Carnegie Mellon University, Pittsburgh, Pennsylvania 15213, USA*
[2]*University of Michigan–Shanghai Jiao Tong University Joint Institute, Shanghai Jiao Tong University, Shanghai 200240, China*

(Received 8 December 2017; published 13 March 2018)

Three models of the $C_{60}$ molecular crystal are studied using molecular dynamics simulations to resolve the roles played by intermolecular and intramolecular degrees of freedom (DOF) in its structural, mechanical, and thermal properties at temperatures between 35 and 400 K. In the full DOF model, all DOF are active. In the rigid body model, the intramolecular DOF are frozen, such that only center of mass (COM) translations and molecular rotations/librations are active. In the point mass model, the molecule is replaced by a point mass, such that only COM translations are active. The zero-pressure lattice constants and bulk moduli predicted from the three models fall within ranges of 0.15 and 20%. The thermal conductivity of the point mass model is the largest across the temperature range, showing a crystal-like temperature dependence (i.e., it decreases with increasing temperature) due to the presence of phonon modes associated with the COM translations. The rigid body model thermal conductivity is the smallest and follows two distinct regimes. It is crystal-like at low temperatures and becomes temperature invariant at high temperatures. The latter is typical of the behavior of an amorphous material. By calculating the rotational diffusion coefficient, the transition between the two regimes is found to occur at the temperature where the molecules begin to rotate freely. Above this temperature, phonons related to COM translations are scattered by the rotational DOF. The full DOF model thermal conductivity is larger than that of the rigid body model, indicating that intramolecular DOF contribute to thermal transport.

DOI: 10.1103/PhysRevB.97.104303

## I. INTRODUCTION

Large unit cell crystals such as fullerenes and their derivatives [1,2], zeolites [3–5], metal-organic frameworks [6–10], superatomic crystals [11,12], clathrates [13,14], and skutterudites [15,16] have attracted interest due to their electronic, optical, mass transport, and thermal properties. The fullerene derivative phenyl-$C_{61}$-butyric acid methyl ester (PCBM), for example, is a promising electron acceptor for organic solar cells due to its high absorption for ultraviolet and visible light and its high electron mobility [17,18]. The thermal conductivity of large unit cell crystals at room temperature is low, typically in the range of 0.01–0.5 W/m K. Low thermal conductivity is beneficial for thermal insulation [19] and thermoelectric energy conversion [20,21]. For other applications, however, low thermal conductivity limits the removal of excess heat, leading to high operating temperatures that degrade performance, reliability, and lifetime [22].

Compared to their electronic, optical, and mass transport properties, the thermal properties of large unit cell crystals have received less attention and are not as well understood. For example, controversy remains regarding the role played by rattler atoms in skutterudites [23–26]. PCBM has the lowest reported thermal conductivity for dense solids, 0.03–0.06 W/m K, but the origin remains unclear [27,28]. The thermal conductivity of the $C_{60}$ molecular crystal, the material that we study here, shows a discontinuity and change in temperature dependence when the rotational degrees of freedom (DOF) are unlocked as the system passes through a first-order phase transition at a temperature of 260 K [29]. This effect was recently shown to have a profound impact on the thermal conductivity of superatomic crystals built from $C_{60}$ and organic-inorganic molecules [12].

The challenge of interpreting experimental measurements and performing detailed modeling of thermal transport in large unit cell crystals is a direct consequence of their complex structure. In an atomic crystal (e.g., silicon, gallium nitride), there are a small number of atoms in the unit cell and the bonding environment is relatively uniform. As such, there are only translational DOF for each atom and thermal transport can be described by the phonon gas model [30]. The small number of atoms in the unit cell allows for the application of accurate solutions of the Boltzmann transport equation using input from first-principles calculations [31–33]. Such calculations are not tractable if the number of atoms in the unit cell is large. Further complications emerge in a molecular crystal like $C_{60}$, where the covalent intramolecular interactions are much stronger than the van der Waals intermolecular interactions [34]. As a consequence, in addition to DOF related to vibrations of individual atoms within molecules (intramolecular DOF), vibrations of the centers of mass of the molecules (translational DOF), and molecular rotations (rotational DOF) are also present and the suitability of the phonon gas model becomes unclear. We will refer to the translational and rotational DOF collectively as the intermolecular DOF.

In the $C_{60}$ molecular crystal, the $C_{60}$ molecules sit on the lattice sites of a face-centered cubic crystal structure [34]. At temperatures above 260 K, the molecules freely rotate and there is rotational disorder [35]. In this regime, thermal conductivity

---

[*] mcgaughey@cmu.edu

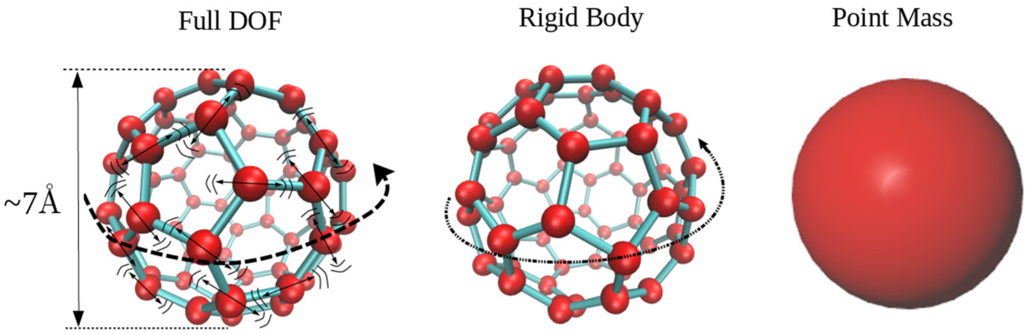

FIG. 1. Our three models for the $C_{60}$ molecule each have a different number of DOF. The full DOF has 180, the rigid body has six, and the point mass has three.

is measured to be temperature-independent (as found in many amorphous materials around room temperature) with a value of 0.4 W/m K [29]. Below this temperature, the rotations are restricted to librations. That is, each $C_{60}$ molecule is locked into an orientationally optimal configuration about which it oscillates [35]. The molecular orientations are correlated and the crystal can be described using a four-molecule basis in a simple cubic crystal structure [35]. In this regime, thermal conductivity increases with decreasing temperature, as found for typical atomic crystals, reaching a value of 1.9 W/m K at the lowest measured temperature of 34 K [29].

The contributions of the intermolecular and intramolecular DOF in $C_{60}$ to thermal transport in the low- and high-temperature regimes are a topic of current research. It has been hypothesized that intermolecular vibrations behave like phonon modes below the phase transition, but are disrupted by the sudden emergence of rotations [29,36]. The role played by the confined, high-frequency intramolecular vibrations, whose occupancy increases with increasing temperature, is also an open question. Do they contribute to thermal transport by carrying energy and/or inhibit it by increasing the scattering of lower-frequency modes?

Previous modeling investigations of thermal transport in $C_{60}$ and its derivative PCBM are limited. Chen *et al.* applied nonequilibrium molecular dynamics (NEMD) simulations to predict their thermal conductivities [37]. They found the thermal conductivity of $C_{60}$ to be system-size dependent, while that for PCBM saturated at a length of 20 nm. They attributed the length-dependent thermal conductivity of $C_{60}$ to the contributions of long-wavelength, low-frequency phonon modes. They explained the low thermal conductivity in PCBM by a reduction in the phonon group velocities and the strong scattering of low-frequency phonons by the alkyl chains. Giri and Hopkins also applied molecular dynamics (MD) simulations to investigate thermal transport in $C_{60}$ and PCBM [38]. Through a spectral analysis method, they asserted that the intermolecular vibrations in $C_{60}$ (i.e., frequencies lower than 3 THz) contribute 65% to the thermal conductivity at a temperature of 300 K, a contribution that increases to 85% when the temperature is decreased to 50 K. In contrast, modes with frequencies less than 3 THz contributed 37% and 40% to the thermal conductivity of PCBM at temperatures of 300 and 50 K.

The objective of this study is to decouple the effects of the intermolecular and intramolecular DOF on thermal transport in $C_{60}$. To do so, three models of $C_{60}$ are considered, as shown in Fig. 1. In the first, called the full DOF model, all DOF (180 per molecule) are active. In the second, called the rigid body model, the intramolecular DOF are frozen such that only the translational and rotational DOF are active (i.e., each $C_{60}$ molecule can only move about its center of mass and rotate). There are thus six DOF per molecule. In the third, called the point mass model, each $C_{60}$ molecule is replaced by an effective point mass such that only the translational DOF are active. There are thus three DOF per molecule.

We perform MD simulations to predict the mechanical and thermal properties predicted by each model between temperatures of 35 and 400 K. Molecular dynamics simulations are classical, such that quantum effects on phonon populations and heat capacity are not included [39]. In fact, the majority of the intramolecular DOF in $C_{60}$ at room temperature are frozen out, suggesting that the rigid body model may be a good approximation under these conditions. Additionally, we use empirical potentials to describe the atomic interactions. Our goal is thus to study general questions of thermal transport in molecular crystals with rotational disorder and not to make a direct comparison to previous experimental measurements.

The remainder of the paper is organized as follows. The interatomic potentials are presented in Sec. II A, including the development of an effective potential for the point mass model. The methodologies for predicting the zero-pressure lattice constant, bulk modulus, rotational diffusion coefficient, and thermal conductivity are provided in Secs. II B to II D. The results are presented in Sec. III, where we assess the suitability of the full DOF, rigid body, and point mass models. The findings are summarized in Sec. IV.

## II. METHODOLOGY

### A. Interatomic potential

The MD simulations were performed using the open-source package LAMMPS [40]. For the full DOF model, the polymer consistent force field (PCFF) was used to model the interatomic interactions [41]. This force field has been parametrized for a wide range of organic compounds by first-principles calculations and includes terms for bonded, angular, dihedral, and nonbonded interactions. The parameters of the intramolecular part of the PCFF are provided in the Supplemental Material (SM) [42]. To be consistent

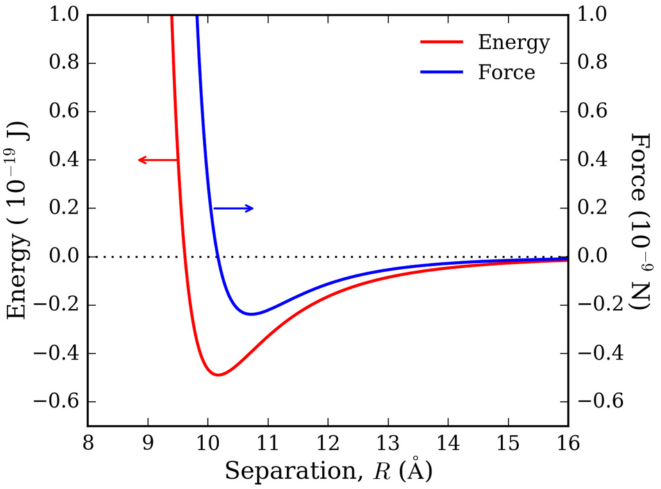

FIG. 2. Effective potential energy and force for the point mass model.

with the PCFF, a 9-6 Lennard-Jones (LJ) potential of the form

$$\phi(r) = \epsilon\left[2\left(\frac{\sigma}{r}\right)^9 - 3\left(\frac{\sigma}{r}\right)^6\right], \tag{1}$$

is used to calculate the potential energy $\phi$ for the nonbonded interaction between two atoms separated by a distance $r$, with $\epsilon = 3.72 \times 10^{-22}$ J, $\sigma = 4.01 \times 10^{-10}$ m, and a cutoff radius of $1.2 \times 10^{-9}$ m. The LJ potential is not applied between atoms on the same molecule. For the rigid body model, only the intermolecular interactions are considered by using Eq. (1).

In the point mass model, each $C_{60}$ molecule is replaced by a point mass with the mass of sixty carbon atoms. The resulting structure is thus a face-centered cubic monoatomic crystal. The interaction between the point masses should be representative of that between two $C_{60}$ molecules. To reproduce this interaction, we placed two $C_{60}$ molecules at a center-to-center separation of $R$, randomized their orientations, and calculated their potential energy using Eq. (1). The orientations were randomized 1000 times for $8 \leqslant R \leqslant 16$ Å in increments of 0.01 Å. The average value of the potential energy at each separation is plotted in Fig. 2 and is taken as the potential energy between two $C_{60}$ molecules in the point mass model. The minimum energy occurs at a separation of 10.2 Å and at a well depth of $4.89 \times 10^{-20}$ J. A two-point forward difference formula is applied to the potential energies to obtain the force, which is also plotted in Fig. 2. The effective potential and force are implemented in LAMMPS using lookup tables that are provided in the SM. The effective point mass interaction between two $C_{60}$ molecules has also been calculated based on a continuum model and a 12-6 LJ potential [43]. A comparison between that model and ours is provided in the SM.

The computational cost decreases in moving from the full DOF model to the rigid body model to the point mass model due to fewer DOF and/or the simpler interatomic potential. For a cubic simulation cell with three unit cells in each direction (which we denote as the $3 \times 3 \times 3$ system and contains 6480 atoms), the wall time on a single core of an AMD Opteron 6128 HE CPU per MD time step is 0.3 s for the full DOF model, 0.16 s for the rigid body model, and $10^{-4}$ s for the point mass model.

### B. Full degree-of-freedom model

The full DOF model has all intermolecular and intramolecular DOF active and uses a time step of 0.3 fs. The structure of an isolated $C_{60}$ molecule is shown in Fig. 1. It has the shape of a truncated icosahedron, comprising twenty hexagons and twelve pentagons. There are two bond types: a double bond common to two hexagons (the 6:6 bond) and a single bond common to a hexagon and a pentagon (the 6:5 bond). The equilibrium structure at zero temperature is provided in the SM. At a temperature of 77 K, the average bond lengths are 1.43 Å (6:6) and 1.50 Å (6:5). The corresponding experimental values at a temperature of 77 K are 1.40 Å (6:6) and 1.45 Å (6:5) [44].

A cubic simulation box with periodic boundary conditions is built by placing the molecular centers of mass at the lattice points of a face-centered cubic crystal. To obtain the zero-pressure lattice constant at a given temperature, we built $2 \times 2 \times 2$ systems (1920 atoms) for 20 lattice constants in increments of 0.001 Å. For each system, $10^5$ time steps of MD simulation were run at constant volume with velocity rescaling to reach the target temperature. The velocity rescaling was then turned off and the simulation was run in the $NVE$ ensemble (i.e., constant number of particles $N$, volume $V$, and energy $E$) for another $6 \times 10^5$ time steps to equilibrate the velocity distribution. The pressure was then collected for $6 \times 10^5$ time steps. The average pressure versus lattice constant data was fitted with a line to obtain the zero-pressure lattice constant.

The bulk modulus, $B$, is obtained using

$$B = -V\frac{dP}{dV}, \tag{2}$$

where $V$ is the system volume and $P$ is its pressure. Using the same methodology as for the zero-pressure lattice constant search, we first predicted the pressure for 20 values of the lattice constant in increments of 0.005 Å around the zero-pressure lattice constant. The average pressure versus volume data was fit with a line that was then used to obtain the bulk modulus from Eq. (2). The same procedure was used for the rigid body and point mass models.

The rotational diffusion coefficient (RDC), $D_r$, is calculated from the autocorrelation of the angular velocities of the $n$ $C_{60}$ molecules through the Green-Kubo formula [45],

$$D_r = \frac{1}{n}\sum_I \int_0^\infty \langle \boldsymbol{\omega}_I(t)\cdot\boldsymbol{\omega}_I(0)\rangle dt, \tag{3}$$

where $\boldsymbol{\omega}_I(t)$ is the angular velocity of molecule $I$ at time $t$. We used a $3 \times 3 \times 3$ system to calculate the RDC. The system is first set to the target temperature through velocity rescaling for $10^5$ steps and then equilibrated in the $NVE$ ensemble for $6 \times 10^5$ steps. The angular velocities of all $C_{60}$ molecules are collected over the following $10^5$ time steps and are used to evaluate Eq. (3). The same procedure is used for the rigid body system.

The thermal conductivity, $k$, for all the three models was predicted using the equilibrium Green-Kubo method [46]. This approach has smaller size effects compared to the NEMD method for a broad range of materials [47], including $C_{60}$ [38]. The Green-Kubo method requires the calculation of the heat flux vector, **q**, which gives the magnitude and direction of the heat flow in the system at an instant in time. For a general multibody potential like PCFF, the heat flux vector is calculated in LAMMPS as [48]

$$\mathbf{q}(t) = \sum_i (e_i \mathbf{v}_i - \mathbf{S}_i \cdot \mathbf{v}_i), \tag{4}$$

where $t$ is time and the summation is over all the atoms $i$ in the system, which have velocity $\mathbf{v}_i$. $e_i$ is the total energy of atom $i$, given by

$$e_i = \tfrac{1}{2} m_i |\mathbf{v}_i|^2 + \phi_i, \tag{5}$$

where $m_i$ and $\phi_i$ are its mass and potential energy. $\mathbf{S}_i$ is the stress tensor for atom $i$, whose definition can be found in the LAMMPS documentation [48].

For a pair (i.e., two-body) potential like LJ, Eqs. (4) and (5) reduce to

$$\mathbf{q}(t) = \sum_i \left[ e_i \mathbf{v}_i + \frac{1}{2} \sum_{j \neq i} (\mathbf{f}_{ij} \cdot \mathbf{v}_i) \mathbf{r}_{ij} \right], \tag{6}$$

$$e_i = \frac{1}{2} m_i |\mathbf{v}_i|^2 + \frac{1}{2} \sum_{j \neq i} \phi_{ij}, \tag{7}$$

where $\mathbf{r}_{ij}$, $\phi_{ij}$, and $\mathbf{f}_{ij}$ are the separation, potential energy, and force between atoms $i$ and $j$.

The thermal conductivity of the cubically isotropic $C_{60}$ system is then predicted from

$$k = \frac{1}{k_B V T^2} \int_0^\infty \frac{\langle \mathbf{q}(t) \cdot \mathbf{q}(0) \rangle}{3} dt, \tag{8}$$

where $k_B$ is the Boltzmann constant, $T$ is temperature, and $\langle \mathbf{q}(\mathrm{t}) \cdot \mathbf{q}(0) \rangle$ is the heat current autocorrelation function (HCACF).

To predict the thermal conductivity of the full DOF system, the temperature is first established using velocity rescaling and the system is equilibrated by running for $10^5$ time steps in the $NVE$ ensemble. The heat flux is then calculated for $2.5 \times 10^6$ time steps in the $NVE$ ensemble. We found good convergence of the integral of the HCACF between correlation times of 10 to 40 ps by averaging over 20 independent simulations (differentiated by random initial velocities). A $3 \times 3 \times 3$ system was found to be sufficient to obtain a size-converged value of thermal conductivity [49]. To estimate the uncertainty, we calculated the thermal conductivity from 19 of the simulations at a time and repeat this process 20 times. The standard deviation of the resulting 20 thermal conductivities is plotted as the error bar.

### C. Rigid body model

The fix/rigid module of LAMMPS was used to run the rigid body simulations [50,51]. To briefly summarize, at every time step, the total force and torque on each molecule is calculated from a summation of the forces and torques on each of its individual atoms. Using the total force and torque, time integration is performed on the center of mass and rotational angles of each molecule. The atomic positions and velocities are then updated such that the molecule translates and rotates as a single entity. As the high-frequency intramolecular vibrational modes are absent in the rigid body model, a large time step of 5 fs is used. The zero-pressure lattice constants found for the full DOF model were used for the rigid body model to ensure the same densities.

To predict the thermal conductivity of the rigid body model, we again used the Green-Kubo method. The major difference between rigid molecules and point particles is their ability to exchange angular momenta and energies in addition to translational momenta and energies. The heat current vector for a set of rigid polyatomic molecules described by a pair potential, as we use here [Eq. (1)], is given by [52,53]

$$\mathbf{q}(t) = \sum_I \left[ e_I \mathbf{V}_I + \frac{1}{2} \sum_{J \neq I} \mathbf{R}_{IJ} (\mathbf{V}_I \cdot \mathbf{F}_{IJ} + \boldsymbol{\omega}_I \cdot \boldsymbol{\Omega}_{IJ}) \right], \tag{9}$$

with

$$e_I = \frac{1}{2} m_I |\mathbf{V}_I|^2 + \frac{1}{2} \boldsymbol{\omega}_I \cdot \mathbf{I}_I \cdot \boldsymbol{\omega}_I + \frac{1}{2} \sum_{J \neq I} \Phi_{IJ}. \tag{10}$$

Here, the summations are over the molecules, labeled by $I$ and $J$, and the lower-case variables from Eqs. (4)–(7) are are replaced by their upper-case counterparts. $\mathbf{I}_I$ is the inertia tensor of molecule $I$ and $\boldsymbol{\Omega}_{IJ}$ is the torque about the center of mass of molecule $I$ due to molecule $J$.

The rigid body system temperature is set by running the simulation in the $NVT$ ensemble (i.e., constant mass, volume, and thermodynamic temperature) with a Nosé-Hoover thermostat for $10^5$ time steps. Equilibration is achieved by running for $10^5$ time steps in the $NVE$ ensemble. The heat current is then calculated for $2 \times 10^5$ time steps in the $NVE$ ensemble and is used to evaluate the thermal conductivity from Eq. (8). A $3 \times 3 \times 3$ system was sufficient to obtain a size-converged value of thermal conductivity [54]. Ten independent simulations (differentiated by random initial velocities) are used to calculate the thermal conductivity. The integral of HCACF is averaged between correlation times of 25 to 50 ps to give the thermal conductivity. The prediction uncertainty was estimated using a similar procedure as described for the full DOF model.

### D. Point mass model

A time step of 20 fs was used for the point mass model simulations. Ten $4 \times 4 \times 4$ systems of different lattice constant were built with an increment in lattice constant of 0.01 Å. The systems were equilibrated to the target temperature in the $NVT$ ensemble using the Langevin thermostat for $10^5$ time steps and then run in the $NVE$ ensemble for $2 \times 10^5$ time steps, during which time the pressure was monitored. At each temperature, the average pressure versus lattice constant data was fit with a line, which was then used to obtain the zero-pressure lattice constant.

To predict thermal conductivity using the Green-Kubo method, a $6 \times 6 \times 6$ system (sufficient to eliminate size effects) was equilibrated by running in the $NVT$ ensemble with the Langevin thermostat for $10^6$ time steps and then equilibrated for $10^6$ time steps in the $NVE$ ensemble. The heat current is collected during another $10^6$ time steps using Eq. (6). Ten independent simulations with random initial conditions were used and the thermal conductivity was extracted by averaging the integral of the HCACF between correlation times of 0.5 to 1 ns. The prediction uncertainty was estimated using a procedure similar to that described for the full DOF model.

## III. RESULTS

### A. Lattice constant and bulk modulus

The zero-pressure lattice constants of the full DOF and point mass models were determined between temperatures of 35 and 400 K. The results are plotted in Fig. 3(a). The predicted lattice constants for the two models deviate by at most 0.02 Å over the temperature range, providing support for the validity of the point mass model. The corresponding densities at a temperature of 300 K are 1609 kg/m$^3$ (full DOF and rigid body) and 1614 kg/m$^3$ (point mass). The experimentally measured density is 1680 kg/m$^3$ [58] and, in a recent simulation study, Giri *et al.* report a density of 1750 kg/m$^3$ [59]. The linear thermal expansion coefficients for the full DOF and point mass models, obtained by fitting a line to all the data for each model, are $1.8 \times 10^{-5}$ K$^{-1}$ and $1.1 \times 10^{-5}$ K$^{-1}$. The full DOF model value is larger because both the intramolecular bond lengths and the molecule-molecule separation distance increase with increasing temperature.

Experimentally measured lattice constants are also plotted in Fig. 3(a) [55]. There is a jump in the data at a temperature of 260 K, which is due to the first-order phase transition [55]. The existence of this phase transition in the MD simulations is explored in Secs. III B and III C. The MD-predicted lattice constants are ∼0.3 Å higher than the experimental values between temperatures of 35 and 260 K. Fitting a line to the experimental data in the temperature range of 50 to 200 K gives a linear thermal expansion coefficient of $1.4 \times 10^{-5}$ K$^{-1}$, which falls in between the predictions from the full DOF and point mass models.

The bulk moduli for the three models are plotted in Fig. 3(b) as a function of temperature along with experimental data [56,57]. The predictions for the three models lie within a range of 20% and are comparable to the experimental values. The bulk modulus of the rigid body model is larger than that of the full DOF model. We attribute this difference to the absence of intramolecular DOF in the rigid body model. A larger pressure is required to strain the material because the molecules themselves are not deformable. The point mass model has a larger bulk modulus than that of the rigid body model, suggesting that the bulk modulus is also related to the relative orientations of the molecules. The bulk moduli of the full DOF and rigid body models show a two-stage linear dependence with a discontinuity in slope around a temperature of 100 K [indicated by the dashed lines in Fig. 3(b)]. As explained in the next section, this temperature roughly corresponds to the free rotation phase transition. Past experiments have also shown that the rotational phase transition gives rise to a discontinuity in the bulk modulus for $C_{60}$ [56,60].

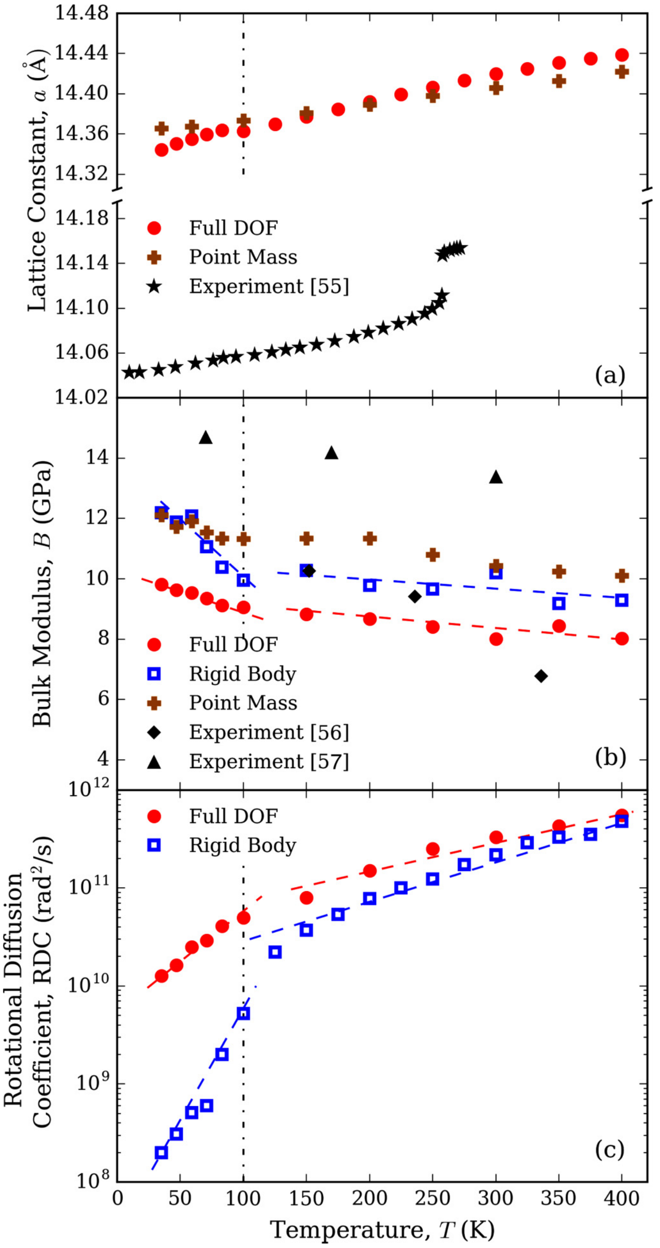

FIG. 3. (a) Lattice constants of the full DOF and point mass models plotted as a function of temperature along with experimental data [55]. (b) Bulk moduli of the three MD models and from experiments [56,57] plotted as a function of temperature. (c) Rotational diffusion coefficient of the full DOF and rigid body models plotted as a function of temperature. The vertical dot-dashed line indicates a temperature of 100 K. The dashed lines in (b) and (c) are to guide the eye.

### B. Rotational diffusional coefficient

The RDCs for the full DOF and rigid body models are plotted in Fig. 3(c) as a function of temperature. Experimental measurements show that the RDC in $C_{60}$ at room temperature is on the order of $10^{11}$ rad$^2$/s [55,61], which is of the same order of magnitude as our simulation results. For both models, the RDC decreases with decreasing temperature. Below a temperature of 100 K, the slopes of both curves increase. The RDC for the rigid body model decreases rapidly, indicating a transition from free rotational motion to orientational freezing [61]. We confirmed this freezing through visualization of the molecular motions.

There is thus a phase transition in the rigid body model around a temperature of 100 K. This temperature is consistent with the temperature at which the bulk modulus (Sec. III A) and thermal conductivity (Sec. III C) also show a change in their temperature dependencies. This temperature is lower than the experimentally-observed phase transition temperature of 260 K. We attribute the difference in the phase transition temperature to the use of Eq. (1). By using a 12-6 LJ potential with parameters adopted from the interlayer interactions in graphite, Cheng and Klein found a phase transition temperature of ∼200 K [62]. Spirk *et al.* [63] found that they could reproduce the experimental transition temperature and low-temperature cage orientations by adding electrostatic interactions between sites placed at the centers of the electron-rich 6:6 bonds.

The full DOF model has a higher RDC than the rigid body model across the entire temperature range and does not show the sharp reduction at low temperatures. Visualization of the $C_{60}$ molecules in the full DOF model shows that they freely rotate at all temperatures considered. Because MD simulations are classical, all DOF are activated at all temperatures. As such, it is easier for the flexible $C_{60}$ molecules in the full DOF model to overcome the potential energy barriers associated with rotations. This behavior may explain why the temperature-dependent rotational behavior of the rigid body model is more similar to experimental observations: the $C_{60}$ molecule is essentially rigid at low temperatures.

### C. Thermal conductivity

We now consider the thermal conductivities of the three models for the $C_{60}$ molecular crystal. The HCACF for all three models at temperatures of 59, 100, 200, 300, and 400 K are provided in the SM. The HCACF integral for each model at a temperature of 300 K is plotted in Fig. 4(a). The longer it takes for the fluctuations in the HCACF to decay, the longer are the lifetimes of the heat carriers [46]. The integrals for the full DOF and rigid body models converge at ∼10 ps, while, for the point mass model, convergence is reached at a time longer than 100 ps. This result indicates the existence of long lifetime modes related to translational DOF in the point mass model that are scattered in the full DOF and rigid body models by rotational and/or intramolecular DOF. The HCACF integral for the full DOF system at a temperature of 300 K is replotted in Fig. 4(b) up to a correlation time of 20 ps. A two-stage behavior is evident that persists at all temperatures, though it becomes less pronounced at lower temperatures. This behavior is not present for the rigid body or point mass models. This particular HCACF integral has a fast initial rise and plateau at 2 ps, followed by a slower increase until it converges to its final value at 10 ps. Based on this observation, we decompose the full DOF model thermal conductivity into two parts: $k_{\mathrm{short}}$ (based on the initial plateau) and $k_{\mathrm{long}}$ (the longer time rise), which are further discussed later in this section. Previous studies have also decomposed thermal conductivity into components based on the timescales associated with the HCACF [64,65].

The thermal conductivity predictions for the three models are plotted in Fig. 5(a) between temperatures of 35 and 400 K. The point mass model has the largest thermal conductivity across the temperature range, followed by the full DOF and the rigid body models. For the point mass model, thermal conductivity decreases monotonically with increasing temperature. This behavior is typical of crystalline materials where thermal transport is dominated by phonons. For such crystals, increasing phonon mode populations with increasing temperature causes more phonon-phonon scattering that leads to a decrease in thermal conductivity. For the full DOF and rigid body models, thermal conductivity decreases with increasing temperature up to 100 K; again, this behavior is typical of a phonon-dominated crystal. Thermal conductivity in these two models is less sensitive to temperature above 100 K, which is typical of an amorphous material. This temperature-dependent behavior of the thermal conductivity of $C_{60}$ is consistent with experimental measurements [36] and previous MD simulations [38].

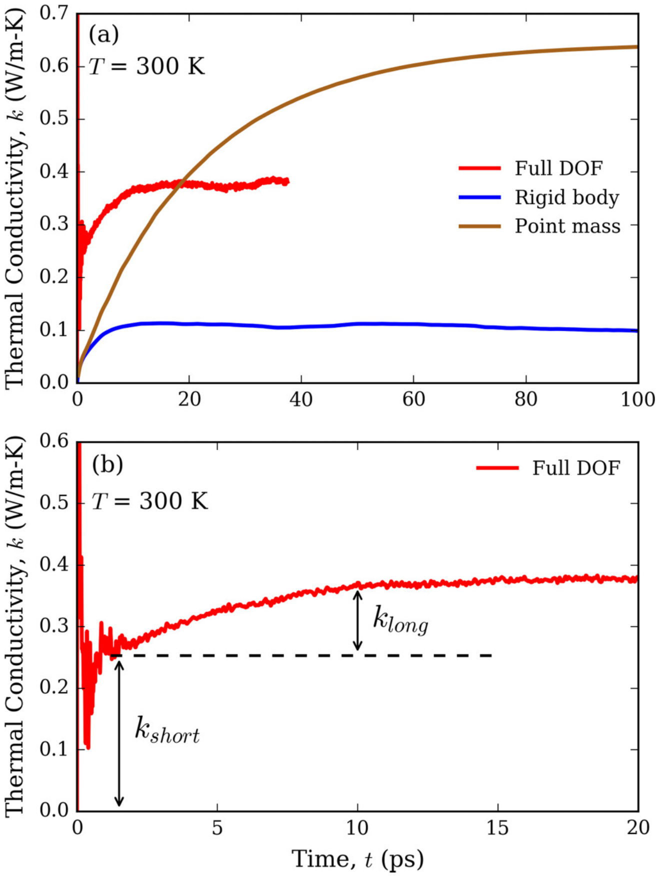

FIG. 4. (a) Integration of the HCACF (i.e., thermal conductivity) for the three $C_{60}$ models at a temperature of 300 K. (b) HCACF for the full DOF model over a shorter time range. $k_{\mathrm{short}}$ and $k_{\mathrm{long}}$ can be distinguished.

To interpret these results, we first compare the point mass and rigid body models. The main difference is that the rigid bodies can rotate/librate while the point masses cannot. The lower thermal conductivity of the rigid body model compared to the point mass model suggests that the rotational DOF, which lead to orientational disorder in the crystal, scatter the long-range, translational phonon-like vibrational modes. This mechanism is consistent with the conclusions of previous

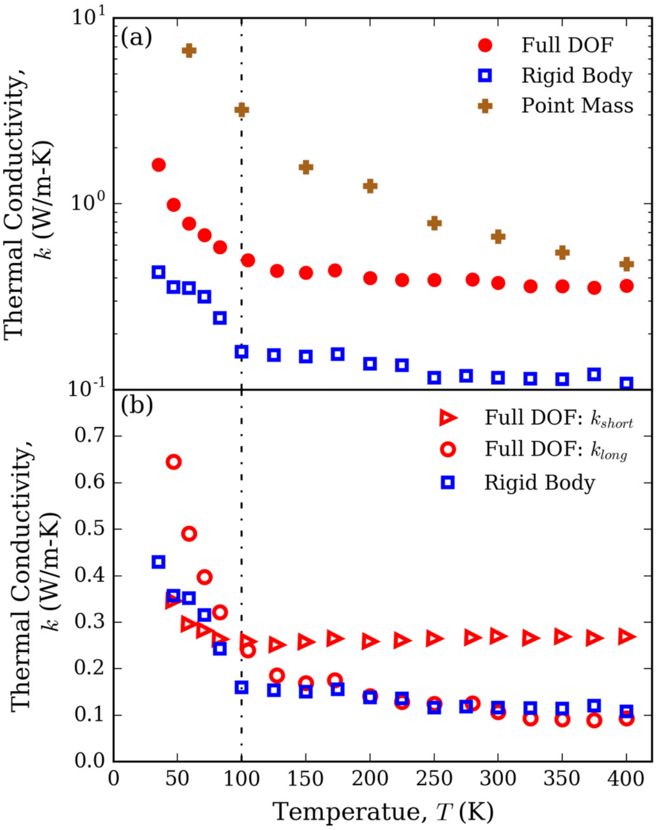

FIG. 5. (a) Thermal conductivity of the three $C_{60}$ models plotted as a function of temperature. (b) Full DOF model thermal conductivity decomposition into $k_{\text{short}}$ and $k_{\text{long}}$ and comparison with the rigid body model. The error bars are smaller than the marker size. The vertical dash-dot line denotes a temperature of 100 K.

studies [12,36]. To support this hypothesis, we note that the discontinuity in slope for the rigid body thermal conductivity occurs at around a temperature of 100 K, which is close to the temperature where there is a sudden change in the RDC, as shown in Fig. 3(c). Above the transition temperature, each molecule is free to rotate and the translational symmetry of the crystal is disrupted, lowering the thermal conductivity. Below the transition temperature, the rotational motions are restricted to librations whose amplitudes decrease with decreasing temperature. In this region, the translational symmetry is preserved and thermal conductivity increases with deceasing temperature.

We also calculated the contributions from the rotational kinetic energy and intermolecular torques to the thermal conductivity based on Eq. (9). The contribution from these two rotational terms is less than 6% and decreases with increasing temperature. We thus conclude that the major effect of rotations in the rigid body model is to scatter energy carriers as opposed to transporting heat.

We now compare the thermal conductivities of the full DOF and rigid body models. The main difference is the presence of the intramolecular DOF in the full DOF model. The full DOF system has a larger thermal conductivity than the rigid body system across the studied temperature range, suggesting that intramolecular vibrations carry heat. To better understand their contribution, we plot $k_{\text{short}}$ and $k_{\text{long}}$ for the full DOF model and the thermal conductivity of the rigid body model, $k_{\text{rigid}}$, in Fig. 5(b).

We hypothesize that $k_{\text{short}}$ and $k_{\text{long}}$ correspond to the contributions of intramolecular and intermolecular DOF to thermal conductivity. The hypothesis can be tested by comparing the magnitudes and temperature dependent behaviors of $k_{\text{long}}$, $k_{\text{short}}$, and $k_{\text{rigid}}$. $k_{\text{long}}$ decreases with increasing temperature and is similar in magnitude to $k_{\text{rigid}}$, particularly at temperatures greater than 100 K, which corresponds to the onset of the molecular rotations. Noting that $k_{\text{rigid}}$ has no contributions from the intramolecular DOF, the similarities between $k_{\text{rigid}}$ and $k_{\text{long}}$ suggest that the latter is a result of the intermolecular vibrations.

On the other hand, $k_{\text{short}}$ shows a temperature-invariant behavior (0.30 ± 0.04 W/m K), which is qualitatively similar to a proposed short-range component in LJ argon [65]. The temperature independence is also similar to the behavior of many amorphous materials around room temperature. This similarity suggests the possibility that, like the diffusons in an amorphous material, intramolecular vibrational modes may contribute to thermal transport via harmonic coupling [66,67]. $k_{\text{short}}$ contributes more than 50% to the thermal conductivity when the temperature is above 100 K, indicating the strong ability of intramolecular vibrations to carry heat. Through an MD-based spectral analysis approach, Giri and Hopkins suggested that the intramolecular vibrations in $C_{60}$ contribute 35% to the thermal conductivity at a temperature of 300 K [38], in the same range as our prediction.

## IV. DISCUSSION AND SUMMARY

We studied three models of the $C_{60}$ molecular crystal (full DOF, rigid body, and point mass, described in Secs. II B–II D) and their impact on its properties. The lattice constants, bulk moduli, and RDCs [Figs. 3(a)–3(c)] predicted from the three models are similar to each other and available experimental data. The results indicate that these structural and mechanical properties strongly depend on the intermolecular interaction between $C_{60}$ molecules [Eq. (1)] and are less sensitive to the intramolecular DOF.

At a temperature of 300 K, the predicted thermal conductivities are 0.62 W/m K (point mass), 0.38 W/m K (full DOF), and 0.12 W/m K (rigid body). Previous MD simulations based on a full DOF model predicted thermal conductivities of 0.20 W/m K from NEMD [37] and 0.27 W/m K from the Green-Kubo method [38] at a temperature of 300 K. Differences compared to our predictions may be a result of the simulation details and different implementations of the PCFF potential [42]. The experimentally measured thermal conductivity is ∼0.4 W/m K at temperatures above 260 K [29]. The agreement between this measured value and the full DOF prediction is likely coincidental. The MD simulations are classical, such that all DOF are active, while the real system will have the majority of the high-frequency modes frozen out due to quantum effects.

The best model for comparison with the experiments is the rigid body model. While the predicted thermal conductivity is lower, the rigid body model shows qualitative features that are consistent with the experiments: notably, that the molecules do not freely rotate below a certain temperature and that thermal conductivity increases with decreasing temperature in this regime. It is challenging to explain the discrepancy in thermal conductivity magnitude and the phase transition temperature because the classical nature of MD and the impact of using empirical potentials are difficult to decouple.

The MD simulations provide important insight into the general behavior of molecular crystals with rotational DOF. Our results suggest that while rotations can scatter phonon-like modes associated with the motions of the molecular center of masses, they do not carry significant heat themselves. Intermolecular interactions and short-range interactions between molecules transport heat, and they do so in a manner that generates a temperature-independent contribution to thermal conductivity. How these mechanisms manifest in more complicated molecular crystals, e.g., PCBM and superatomic crystals, is an intriguing direction for future study.

## ACKNOWLEDGMENTS

We thank Kevin D. Parrish and Jonathan A. Malen (Carnegie Mellon University) for helpful discussions and insights. This work was supported by the NSF Award DMR-1507325. C.S. acknowledges the financial support from a program of the China Scholarships Council.

S.K. and C.S. contributed equally to this work.

---

[1] M. S. Dresselhaus, G. Dresselhaus, and P. C. Eklund, *Science of Fullerenes and Carbon nanotubes: Their Properties and Applications* (Academic, New York, 1996).

[2] M. T. Dang, L. Hirsch, and G. Wantz, Adv. Mater. **23**, 3597 (2011).

[3] Y. Tao, H. Kanoh, L. Abrams, and K. Kaneko, Chem. Rev. **106**, 896 (2006).

[4] A. J. H. McGaughey and M. Kaviany, Int. J. Heat Mass Transfer **47**, 1799 (2004).

[5] B. M. Weckhuysen and J. Yu, Chem. Soc. Rev. **44**, 7022 (2015).

[6] H. Li, M. Eddaoudi, M. O'Keeffe, and O. M. Yaghi, Nature (London) **402**, 276 (1999).

[7] B. L. Huang, A. J. H. McGaughey, and M. Kaviany, Int. J. Heat Mass Transf. **50**, 393 (2007).

[8] B. L. Huang, Z. Ni, A. Millward, A. J. H. McGaughey, C. Uher, M. Kaviany, and O. Yaghi, Int. J. Heat Mass Transf. **50**, 405 (2007).

[9] J. Lee, O. K. Farha, J. Roberts, K. A. Scheidt, S. T. Nguyen, and J. T. Hupp, Chem. Soc. Rev. **38**, 1450 (2009).

[10] H. Babaei, A. J. H. McGaughey, and C. E. Wilmer, Chem. Sci. **8**, 583 (2017).

[11] X. Roy, C.-H. Lee, A. C. Crowther, C. L. Schenck, T. Besara, R. A. Lalancette, T. Siegrist, P. W. Stephens, L. E. Brus, P. Kim *et al.*, Science **341**, 157 (2013).

[12] W.-L. Ong, E. S. O'Brien, P. S. M. Dougherty, D. W. Paley, C. F. Higgs III, A. J. H. McGaughey, J. A. Malen, and X. Roy, Nat. Mater. **16**, 83 (2017).

[13] G. Nolas, J. Cohn, G. Slack, and S. Schujman, Appl. Phys. Lett. **73**, 178 (1998).

[14] R. Ross, P. Andersson, and G. Bäckström, Nature (London) **290**, 322 (1981).

[15] G. Nolas, D. Morelli, and T. M. Tritt, Annu. Rev. Mater. Sci. **29**, 89 (1999).

[16] V. Keppens, D. Mandrus, B. Sales, B. Chakoumakos *et al.*, Nature (London) **395**, 876 (1998).

[17] P. W. Blom, V. D. Mihailetchi, L. J. A. Koster, and D. E. Markov, Adv. Mater. **19**, 1551 (2007).

[18] G. Li, R. Zhu, and Y. Yang, Nat. Photonics **6**, 153 (2012).

[19] N. P. Padture, M. Gell, and E. H. Jordan, Science **296**, 280 (2002).

[20] A. I. Boukai, Y. Bunimovich, J. Tahir-Kheli, J.-K. Yu, W. A. Goddard Iii, and J. R. Heath, Nature (London) **451**, 168 (2008).

[21] M. S. Dresselhaus, G. Chen, M. Y. Tang, R. Yang, H. Lee, D. Wang, Z. Ren, J.-P. Fleurial, and P. Gogna, Adv. Mater. **19**, 1043 (2007).

[22] E. Pop, Nano Res. **3**, 147 (2010).

[23] G. Nolas, G. Slack, D. Morelli, T. Tritt, and A. Ehrlich, J. Appl. Phys. **79**, 4002 (1996).

[24] G. S. Nolas, J. L. Cohn, and G. A. Slack, Phys. Rev. B **58**, 164 (1998).

[25] B. C. Sales, B. C. Chakoumakos, and D. Mandrus, Phys. Rev. B **61**, 2475 (2000).

[26] H. Kim, M. Kaviany, J. C. Thomas, A. Van der Ven, C. Uher, and B. Huang, Phys. Rev. Lett. **105**, 265901 (2010).

[27] J. C. Duda, P. E. Hopkins, Y. Shen, and M. C. Gupta, Phys. Rev. Lett. **110**, 015902 (2013).

[28] X. Wang, C. D. Liman, N. D. Treat, M. L. Chabinyc, and D. G. Cahill, Phys. Rev. B **88**, 075310 (2013).

[29] R. C. Yu, N. Tea, M. B. Salamon, D. Lorents, and R. Malhotra, Phys. Rev. Lett. **68**, 2050 (1992).

[30] J. M. Ziman, *Electrons and Phonons: The Theory of Transport Phenomena in Solids* (Oxford University Press, Oxford, 1960).

[31] D. Broido, M. Malorny, G. Birner, N. Mingo, and D. Stewart, Appl. Phys. Lett. **91**, 231922 (2007).

[32] K. Esfarjani, G. Chen, and H. T. Stokes, Phys. Rev. B **84**, 085204 (2011).

[33] L. Lindsay, D. A. Broido, and T. L. Reinecke, Phys. Rev. B **87**, 165201 (2013).

[34] W. I. David, R. M. Ibberson, J. C. Matthewman, K. Prassides, T. J. S. Dennis, J. P. Hare, H. W. Kroto, R. Taylor, and D. R. Walton, Nature (London) **353**, 147 (1991).

[35] W. David, R. Ibberson, T. Dennis, J. Hare, and K. Prassides, Europhys. Lett. **18**, 219 (1992).

[36] N. Tea, R.-C. Yu, M. Salamon, D. Lorents, R. Malhotra, and R. Ruoff, Appl. Phys. A **56**, 219 (1993).

[37] L. Chen, X. Wang, and S. Kumar, Sci. Rep. **5**, 12763 (2015).

[38] A. Giri and P. E. Hopkins, J. Phys. Chem. Lett. **8**, 2153 (2017).

[39] J. E. Turney, A. J. H. McGaughey, and C. H. Amon, Phys. Rev. B **79**, 224305 (2009).

[40] S. Plimpton, J. Comput. Phys. **117**, 1 (1995).

[41] H. Sun, S. J. Mumby, J. R. Maple, and A. T. Hagler, J. Am. Chem. Soc. **116**, 2978 (1994).

[42] See Supplemental Material at http://link.aps.org/supplemental/10.1103/PhysRevB.97.104303 for information about our implementation of PCFF in LAMMPS, the equilibrium structure of a $C_{60}$ molecule at zero temperature, the lookup tables for the effective potential and force for the point mass model, the comparison of our point mass model with one from the former literature, and

the HCACF of three models at temperatures of 59, 100, 200, 300, and 400 K.

[43] L. A. Girifalco, M. Hodak, and R. S. Lee, Phys. Rev. B **62**, 13104 (2000).

[44] C. S. Yannoni, P. P. Bernier, D. S. Bethune, G. Meijer, and J. R. Salem, J. Am. Chem. Soc. **113**, 3190 (1991).

[45] B.-Y. Cao and R.-Y. Dong, J. Chem. Phys. **140**, 034703 (2014).

[46] A. J. H. McGaughey and M. Kaviany, Adv. Heat Transfer **39**, 169 (2006).

[47] D. P. Sellan, E. S. Landry, J. E. Turney, A. J. H. McGaughey, and C. H. Amon, Phys. Rev. B **81**, 214305 (2010).

[48] http://lammps.sandia.gov.

[49] We ran test cases for the full DOF model at a temperature of 300 K with a lattice constant of 14.42 Å. For $2 \times 2 \times 2$, $3 \times 3 \times 3$, and $4 \times 4 \times 4$ systems, the thermal conductivities are $0.309 \pm 0.006$, $0.377 \pm 0.005$, and $0.376 \pm 0.005$ W/m K.

[50] T. Miller Iii, M. Eleftheriou, P. Pattnaik, A. Ndirango, D. Newns, and G. Martyna, J. Chem. Phys. **116**, 8649 (2002).

[51] H. Kamberaj, R. Low, and M. Neal, J. Chem. Phys. **122**, 224114 (2005).

[52] D. J. Evans, Mol. Phys. **32**, 1171 (1976).

[53] D. J. Evans and W. B. Streett, Mol. Phys. **36**, 161 (1978).

[54] We ran test cases for the rigid body model at a temperature of 300 K with a lattice constant of 14.44 Å. For $2 \times 2 \times 2$, $3 \times 3 \times 3$, and $4 \times 4 \times 4$ systems, the thermal conductivities are $0.088 \pm 0.002$, $0.133 \pm 0.003$, and $0.137 \pm 0.002$ W/m K.

[55] W. David, R. Ibberson, and T. Matsuo, Proc. R. Soc. London A **442**, 129 (1993).

[56] A. Lundin and B. Sundqvist, Europhys. Lett. **27**, 463 (1994).

[57] H. Ludwig, W. Fietz, F. Hornung, K. Grube, B. Wagner, and G. Burkhart, Z. Phys. B: Condens. Matter **96**, 179 (1994).

[58] W. Krätschmer, L. D. Lamb, K. Fostiropoulos, and D. R. Huffman, Nature (London) **347**, 354 (1990).

[59] A. Giri and P. E. Hopkins, Phys. Rev. B **96**, 220303 (2017).

[60] L. Pintschovius, O. Blaschko, G. Krexner, and N. Pyka, Phys. Rev. B **59**, 11020 (1999).

[61] R. D. Johnson, C. S. Yannoni, H. C. Dorn, J. R. Salem, and D. S. Bethune, Science **255**, 1235 (1992).

[62] A. Cheng and M. L. Klein, J. Phys. Chem. **95**, 6750 (1991).

[63] M. Sprik, A. Cheng, and M. L. Klein, J. Phys. Chem. **96**, 2027 (1992).

[64] J. Che, T. Çağın, W. Deng, and W. A. Goddard III, J. Chem. Phys. **113**, 6888 (2000).

[65] A. J. H. McGaughey and M. Kaviany, Int. J. Heat Mass Transfer **47**, 1783 (2004).

[66] P. B. Allen and J. L. Feldman, Phys. Rev. B **48**, 12581 (1993).

[67] J. M. Larkin and A. J. H. McGaughey, Phys. Rev. B **89**, 144303 (2014).